Astronomy & Astrophysics

The fountain of the luminous infrared galaxy Zw049.057 as traced by its OH megamaser

Boy Lankhaar[1,2,★], Susanne Aalto[1], Clare Wethers[1], Javier Moldon[3,4], Rob Beswick[4], Mark Gorski[1],
Sabine König[1], Chentao Yang[1], Jeff Mangum[5], John Gallagher[6,7], Françoise Combes[8],
Dimitra Rigopoulou[9,10], Eduardo González-Alfonso[11], Sébastien Muller[1], Ismael Garcia-Bernete[9],
Christian Henkel[12], Yuri Nishimura[13], and Claudio Ricci[14,15]

1 Department of Space, Earth and Environment, Chalmers University of Technology, Onsala Space Observatory, 439 92 Onsala, Sweden
2 Leiden Observatory, Leiden University, Post Office Box 9513, 2300 RA Leiden, The Netherlands
3 Instituto de Astrofísica de Andalucía, Glorieta de la Astronomía, s/n, 18008 Granada, Spain
4 Jodrell Bank Centre for Astrophysics, Department of Physics and Astronomy, The University of Manchester, Manchester M13 9PL, UK
5 National Radio Astronomy Observatory, 520 Edgemont Road, Charlottesville, VA 22903, USA
6 Wisconsin IceCube Particle Astrophysics Center, Madison, WI 53703, USA
7 Department of Physics and Astronomy, Macalester College, 1600 Grand Ave, St. Paul, MN 55105, USA
8 Observatoire de Paris, LERMA, Collège de France, CNRS, PSL University, Sorbonne University, Paris, France
9 Astrophysics, Department of Physics, University of Oxford, Keble Road, Oxford OX1 3RH, UK
10 School of Sciences, European University Cyprus, Diogenes Street, Engomi, 1516 Nicosia, Cyprus
11 Universidad de Alcalá, Departamento de Física y Matemáticas, Campus Universitario, 28871 Alcalá de Henares, Madrid, Spain
12 Max-Planck-Institut für Radioastronomie Auf dem Hügel 69, 53121 Bonn, Germany
13 Department of Astronomy, The University of Tokyo, 7-3-1, Hongo, Bunkyo, Tokyo 113-0033, Japan
14 Instituto de Estudios Astrofísicos, Facultad de Ingeniería y Ciencias, Universidad Diego Portales, Av. Ejército Libertador 441, Santiago, Chile
15 Kavli Institute for Astronomy and Astrophysics, Peking University, Beijing 100871, China

ABSTRACT

High-resolution ($0\overset{''}{.}037-0\overset{''}{.}13$ [10−35 pc]) e-MERLIN ($\lambda 6-18$ cm) and ($0\overset{''}{.}024$ [6.5 pc]) ALMA ($\lambda 1.1$ mm) observations have been used to image OH (hydroxyl) and H_2CO (formaldehyde) megamaser emission, and HCN 3 → 2 emission toward the nuclear (<100 pc) region of the luminous infrared galaxy Zw049.057. Zw049.057 hosts a compact obscured nucleus (CON), and thus represents a class of galaxies that are often associated with inflow and outflow motions. Formaldehyde megamaser emission has been detected toward the nuclear region, $\lesssim 30$ pc ($0\overset{''}{.}1$), and traces a structure along the disk major axis. OH megamaser (OHM) emission has been detected along the minor axis of the disk, ∼30 pc ($0\overset{''}{.}1$) from the nucleus, where it exhibits a velocity gradient with extrema of −20 km s^{-1} southeast (SE) of the disk and −110 km s^{-1} northwest (NW) of the disk. HCN 3 → 2 emission reveals extended emission, along the disk minor axis out to ∼60 pc ($0\overset{''}{.}2$). Analysis of the minor axis HCN emission reveals high-velocity features extending out to 600 km s^{-1}, redshifted on the SE side and blueshifted on the NW side. We propose that the high-velocity HCN emission traces a fast (>250 km s^{-1}) and collimated outflow that is enveloped by a wide-angle and slow (∼50 km s^{-1}) outflow that is traced by the OHM emission. Analysis of the outflow kinematics suggests that the slow wide-angle outflow will not reach escape velocity and will instead fall back to the galaxy disk, evolving as a so-called fountain flow, while the fast collimated outflow traced by HCN emission will likely escape the nuclear region. We suggest that the absence of OHM emission in the nuclear region is due to high densities there. Even though OHMs associated with outflows are an exception to conventional OHM emission, we expect them to be common in CON sources that host both OHM and H_2CO megamasers.

Key words. masers – ISM: jets and outflows – galaxies: evolution – galaxies: ISM – galaxies: kinematics and dynamics – galaxies: nuclei

1. Introduction

The majority of the most luminous galaxies radiate the bulk of their energy in the far-infrared (FIR, Sanders & Mirabel 1996). According to their luminosity, these are either classified as luminous ($L_{IR} > 10^{11}$ L$_\odot$) infrared galaxies (LIRGs), or ultra-luminous ($L_{IR} > 10^{12}$ L$_\odot$) infrared galaxies (ULIRGs). The extreme luminosities of (U)LIRGs are powered by an active galactic nucleus (AGN), an intense starburst (SB) phase, or both. (U)LIRGs emit the bulk of their energy in the FIR as their luminosity sources are embedded in a dusty phase that reprocesses radiation to longer wavelengths. While (U)LIRGs represent an evolutionary phase that many galaxies go through (e.g. Smail et al. 1997; Hughes et al. 1998), they themselves are rapidly evolving objects.

★ Corresponding author; boy.lankhaar@chalmers.se

A significant fraction of (U)LIRGs host compact ($r <$ 100 pc), highly obscured ($N_{H_2} \gtrsim 10^{25}$ cm^{-2}), and warm ($T \gtrsim$ 100 K) nuclei (Aalto et al. 2015b; Falstad et al. 2019, 2021; García-Bernete et al. 2022; Donnan et al. 2023). These compact obscured nuclei (CONs) are responsible for a large fraction of the total infrared luminosity of their host galaxies, despite their small sizes (González-Alfonso et al. 2012; Falstad et al. 2015, 2021). Due to their opaque nature, it is difficult to discern the ultimate source of their luminosity. It has become increasingly clear that the CONs represent an evolutionary phase that is associated with both inflowing (González-Alfonso et al. 2017; Aalto et al. 2019; Falstad et al. 2019) and outflowing (Barcos-Muñoz et al. 2018; Falstad et al. 2018; Gorski et al. 2023; Wethers et al. 2024) gas motions. Yet, due to their opaqueness, signatures of radial gas motions are often only discernible at wavelengths $\gtrsim$1 mm (Falstad et al. 2019).

Radial gas motions toward galaxy nuclei are decidedly important to understanding galaxy evolution. Inflowing gas motions drive nuclear activity and feed the nuclear star-forming gas. In turn, outflows transport the chemically enriched nuclear gas and dust away from the nuclear region, toward galaxy halos and the intergalactic medium (Veilleux et al. 2020; Martin 2005), but also may contribute to nuclear growth by efficiently transporting angular momentum (Wada 2012; Konigl & Kartje 1994). Galactic outflows may be driven by nuclear activity, stellar winds and supernovae from the SB phase, radiation pressure, or cosmic-ray pressure (Veilleux et al. 2020). Indeed, the association of CONs with radial gas motions indicates that these sources are rapidly evolving (Sakamoto et al. 2013). Understanding these gas motions and constraining their driving mechanism(s) is of pivotal importance to understanding CONs, both as a subclass of (U)LIRGs, as well as their individual relations with their host galaxies.

In this work, we study gas kinematics toward the galaxy Zw049.057 (IRAS 15107+0724). Zw049.057 is a LIRG, with a luminosity of $L_{IR} = 1.8 \times 10^{11}$ L$_\odot$, located ([RA, Dec] (J2000) = [15:13:13.10 +07:13:32.0]) at an estimated distance of 56 Mpc (Sanders et al. 2003), and hosts a CON (Aalto et al. 2015b; Falstad et al. 2021). We adopt a redshift of $z = 0.01299$, which corresponds to a systemic velocity of 3897 km s^{-1} (Katgert et al. 1998). Throughout this paper, the optical velocity convention is used with respect to the barycentric reference frame. It is an OHM galaxy (Baan et al. 1987; McBride et al. 2013), with evidence of inflows (Falstad et al. 2015) and outflow structures (Baan et al. 1987; Falstad et al. 2018), heavily obscured in the nuclear region (Falstad et al. 2019). The major axis of the nuclear disk has a position angle of PA$_{maj}$ = 210° (Falstad et al. 2018). We present ALMA observations of the HCN $J = 3 \rightarrow 2$ emission, that show signatures of a collimated outflowing structure, and e-MERLIN observations of OHM and H$_2$CO (formaldehyde) emission toward Zw049.057. We find evidence that the OHM emission is associated with an outflow structure, while population inversion, and thus the OHM emission, is suppressed in the nuclear disk region.

OH megamasers are hosted by (U)LIRGs, where they are commonly taken to represent a compact and intense mode of star formation, that is likely triggered by tidal density enhancements due to merger events (Darling 2007; Darling & Giovanelli 2002). The picture of Darling (2007) is indeed consistent with modeling efforts (Parra et al. 2005; Lockett & Elitzur 2008) as well as previous high-angular-resolution imaging of the more luminous OHM using Very Long Baseline Interferometry (VLBI) instruments (Lonsdale et al. 1998; Pihlström et al. 2001; Richards et al. 2005). This picture, though, is in ten-

sion with the association of OHM with an outflow structure; a feature of OHM that has been identified in an increasing number of sources (Baan et al. 1987, 1989; Gowardhan et al. 2018). We explore this tension in detail by comparing resolved e-MERLIN imaging of the H$_2$CO megamaser of Zw049.057 with the resloved imaging of the OHM, and analyzing their (dis)association on the basis of previous excitation modeling (van der Walt et al. 2007; van der Walt & Mfulwane 2022; Lockett & Elitzur 2008), as well as the emerging picture of the inner dynamics of CON regions (Aalto et al. 2012; Falstad et al. 2019, 2021; Gorski et al. 2023).

This paper is structured as follows. In Section 2, we present the observational setups that were used. In Section 3, we describe the results of our observations. In Section 4, we discuss our results, in which we lay emphasis on the outflow dynamics, as well as the implication of our results for the class of OH megamasers. We present our conclusions in Section 5.

2. Observations

2.1. e-MERLIN observations

Zw049.057 was observed with the e-MERLIN array between January 7-14, 2019 in the L-band (project code CY7222) and January 7-8, 2018 in the C-band (CY6203). Observations included all e-MERLIN Telescopes, except the Lovell Telescope (six telescopes in total). L-band observations were correlated into eight 64-MHz wide spectral windows spanning a total frequency range of 1245–1757 MHz. At C-band observations encompassed 4488–5000 MHz, correlated into four spectral windows. A total of 17.25 and 14.8 hours of observations were used at L-band and C-band, respectively.

Correlators were set to the C-band 4829 MHz H$_2$CO $J_{K_a K_c} = 1_{10}$-1_{11}-transition and to the L-band 1667 and 1665 MHz OH transitions. The flux calibrator was 3C286 and the baseline calibrator OQ208 for both sets of observations. Nearby gain calibrators 1516+0701 and 1513+0713 were used in the L and C bands, respectively.

Data were initially processed using NRAO's CASA (Bean et al. 2022) using the e-MERLIN pipeline[1] (Moldon 2021), which applies flagging, delay and bandpass calibration, and calculates phase and frequency-dependent amplitude gain corrections. Following initial calibration observing bands centered on the redshifted frequencies of the OH (1665 and 1667 MHz rest frequency) and H$_2$CO (4830 MHz rest frequency) lines were extracted and imaged to form individual spectral line cubes for further analysis.

The synthesized beams are $0\rlap{.}''11 \times 0\rlap{.}''039$ (30×11 pc) for the H$_2$CO observations and $0\rlap{.}''26 \times 0\rlap{.}''13$ (70.6×35.3 pc) for the OH observations. The resulting data have a sensitivity of 0.2 mJy per beam in a 64 km s^{-1} (1 MHz) channel width (H$_2$CO) and 0.77 mJy per beam in a 20 km s^{-1} (0.11 MHz) channel width (OH).

2.2. ALMA observations

Observations were carried out with 42 antennas in the array configuration C43-9/10, with projected baselines between 92 m and 13.8 km, on August 28, 2021. The on-source integration time was 34 minutes under relatively good atmospheric conditions (amount of precipitable water vapor $PWV \sim 0.5$ mm).

---

[1] https://github.com/e-merlin/eMERLIN_CASA_pipeline

The bandpass response of the individual antennas was determined from the quasar $J1550+0527$. The quasar $J1521+0420$ was observed regularly for gain calibration. The absolute flux scale was calibrated using the quasar $J1550+0527$. The flux density for $J1550+0527$ was taken from the ALMA flux calibrator database.

The correlator was set up to cover four spectral windows in Band 6. The first two spectral windows were assigned to the upper side band, with bandwidths of 1.875 GHz and a spectral resolution of 7.8 MHz, to cover the HCO^+ $J = 3 \rightarrow 2$ and vibrationally excited HCN $J = 3 \rightarrow 2$ ν_2 = 1f lines (spectral window centered at a sky frequency 264.3 GHz) and the HCN $J = 3 \rightarrow 2$ line in the ground vibrational state (spectral window centered at 262.5 GHz). Two additional 2-GHz wide spectral windows were assigned to the lower side band, with a coarser spectral resolution of 31.25 MHz, to sample the continuum emission.

All of the ALMA Band 6 observations of Zw049.057 will be published in an upcoming paper by Wethers et al. (priv. comm.). Here, we present some results on HCN $J = 3 \rightarrow 2$.

The synthesized beam is $0\farcs027 \times 0\farcs024$ (7.33×6.52 pc), where Briggs weighting was used, adopting a robust parameter of 0.5. The resulting data have a sensitivity of 0.26 mJy per beam in a 20 km s^{-1} (18 MHz) channel width.

3. Results

3.1. L band continuum

The L band continuum around 1.67 GHz (λ18 cm) was detected toward the nuclear region of Zw049.057; a contour map is given in Fig. 1d. Continuum emission was found to exhibit extended features in the direction roughly perpendicular to the nuclear disk major axis, with a position angle of PA$_{C \text{ exten.}}$ = 120°. The maximum flux density was observed as 21.5 ± 0.4 mJy beam^{-1}. We used the Rayleigh-Jeans law to obtain a corresponding brightness temperature of 3.25×10^5 K. The spatially integrated total flux density toward the nuclear region was $S_\nu = 41.4 \pm 4$ mJy, which can be compared to Arecibo single dish observations that retrieve an 18 cm continuum flux of 40 ± 5 mJy (Baan et al. 1987). Half of the total continuum emission emanates from an (angular) area of 0.05 arcsec^2 (60 pc^2). We note that this area is very similar to the area of emittance of 33 GHz continuum radiation, $A_{33 \text{ GHz}}$ = 0.031 arcsec^2, as has been found by Song et al. (2022).

3.2. OH megamaser (OHM)

OHM emission was detected toward the nuclear region of Zw049.057 in both the 1.667 GHz and the 1.665 GHz transitions. For the main maser transition at 1.667 GHz, we retrieved an integrated total flux of 2.0 ± 0.4 Jy km s^{-1}, while for the satellite maser transition at 1.665 GHz, we retrieved 1.0 ± 0.2 Jy km s^{-1}. The total integrated flux of the 1.667 GHz maser compares well to Baan et al. (1987), who find 2.25 Jy km s^{-1} and McBride et al. (2013), who find 2.45 Jy km s^{-1}[2]. The integrated total flux corresponds to an OH luminosity of $L_{OH} = 10.1$ $L_\odot$. Figure 1e shows the moment 0 map of the 1.667 GHz OHM emission. OHM emission is observed near the minor axis, with maximal emis-

sion appearing about $0\farcs2$ (~57 pc) from the 18 cm continuum peak. The emission to the west of the continuum peak appears stronger, compared to the emission to the east of the continuum peak. Emission toward the nucleus, as well as along the major axis, is undetected. The moment 1 map of the 1.667 GHz OHM emission, given in Fig. 1f shows a clear velocity gradient, from -20 km s^{-1} in the east, to -100 km s^{-1} in the west (corresponding to about 5 spectral channels). Within the northwest (NW) OHM feature, a velocity gradient from the north to the south is observed, but we note that this feature occurs on a scale smaller than the beam size. The velocity dispersion, taken as the square root of the moment 2 map of the 1.667 GHz OHM emission, given in Fig. 1g, appears constant around 70 km s^{-1} throughout the OHM region.

Imaging of the 1.665 GHz transition is given in Fig. A.2. It is readily apparent that the NW feature of the OHM main line is also found for the weaker 1.665 GHz maser line; the moment 0 image shows a feature at a similar position, while the moment 1 map shows a similar velocity field compared to the main maser transition at 1.667 GHz. We do not detect the southeast (SE) feature of the OHM emission. We ascribe this to sensitivity effects as for the main maser line, this feature was also considerably weaker.

3.3. C band continuum

The C band continuum around 4.8 GHz (λ6.2 cm) was detected toward the nuclear region of Zw049.057. In Fig. 1a we display a contour map of the C band continuum. As for the L band continuum, an extended structure appears present along the minor axis (P.A. of ~120°). The maximum spectral flux density we observed as 12.0 ± 0.1 mJy/beam, corresponding to a brightness temperature of 1.68×10^5 K. We retrieved an integrated total flux density toward the nuclear region that was observed as $S_\nu = 25.6 \pm 2$ mJy, which compares well to the MERLIN observations of Baan et al. (2017) that retrieved 29.72 mJy, as well as the Arecibo observations of Araya et al. (2004) that retrieved 30.8 mJy. Half of the total e-MERLIN C band continuum emission emanates from an (angular) area of 0.008 arcsec^2 (20 pc).

3.4. H_2CO megamaser

H_2CO megamaser emission was detected toward the nucleus of Zw049.057 in the $(J_{K_a,K_c} \rightarrow J'_{K'_a,K'_c})$ $1_{1,0} \rightarrow 1_{1,1}$ transition at 4.83 GHz. Figs. 1b and 1c present the moment 0 and 1 maps of the detected emission, while a zoom-in of these figures can be found in Fig. A.1. Maximal emission was found at 1.08 mJy beam^{-1}, corresponding to 1.4×10^4 K. We retrieved an integrated total flux of 0.48 ± 0.04 Jy km s^{-1}, where Baan et al. (2017) finds 0.308 Jy km s^{-1} using MERLIN and Araya et al. (2004) find 0.283 Jy km s^{-1} using Arecibo. From the integrated total flux, we computed the corresponding maser luminosity 7.3 ± 0.6 $L_\odot$, which is large enough for it to fulfill the threshold to be considered megamaser emission[3]. Figure 1b shows the moment 0 map of the 4.83 GHz H_2CO emission. H_2CO emission is observed concentrated along the major axis (PA ~ 210°, Falstad et al. 2018), with maximal emission appearing about $0\farcs1$ (~29 pc) NE of the 6.2 cm continuum peak. Emission to the north of the 6.2 cm continuum peak appears ~25% stronger than the emission to the south of the C band continuum peak. The moment 1 map of the emission, shown in Fig. 1c shows a velocity gradient, red to blue, from north to south.

---

[2] We note McBride et al. (2013) report an integrated flux 4.9 Jy km s^{-1}. However, as explained in McBride et al. (2013) they use a different definition of the total flux density resulting in a factor two increase in the reported flux density compared to commonly used definitions including those used in this paper. For a deeper discussion surrounding this topic, we refer to Robishaw & Heiles (2021).

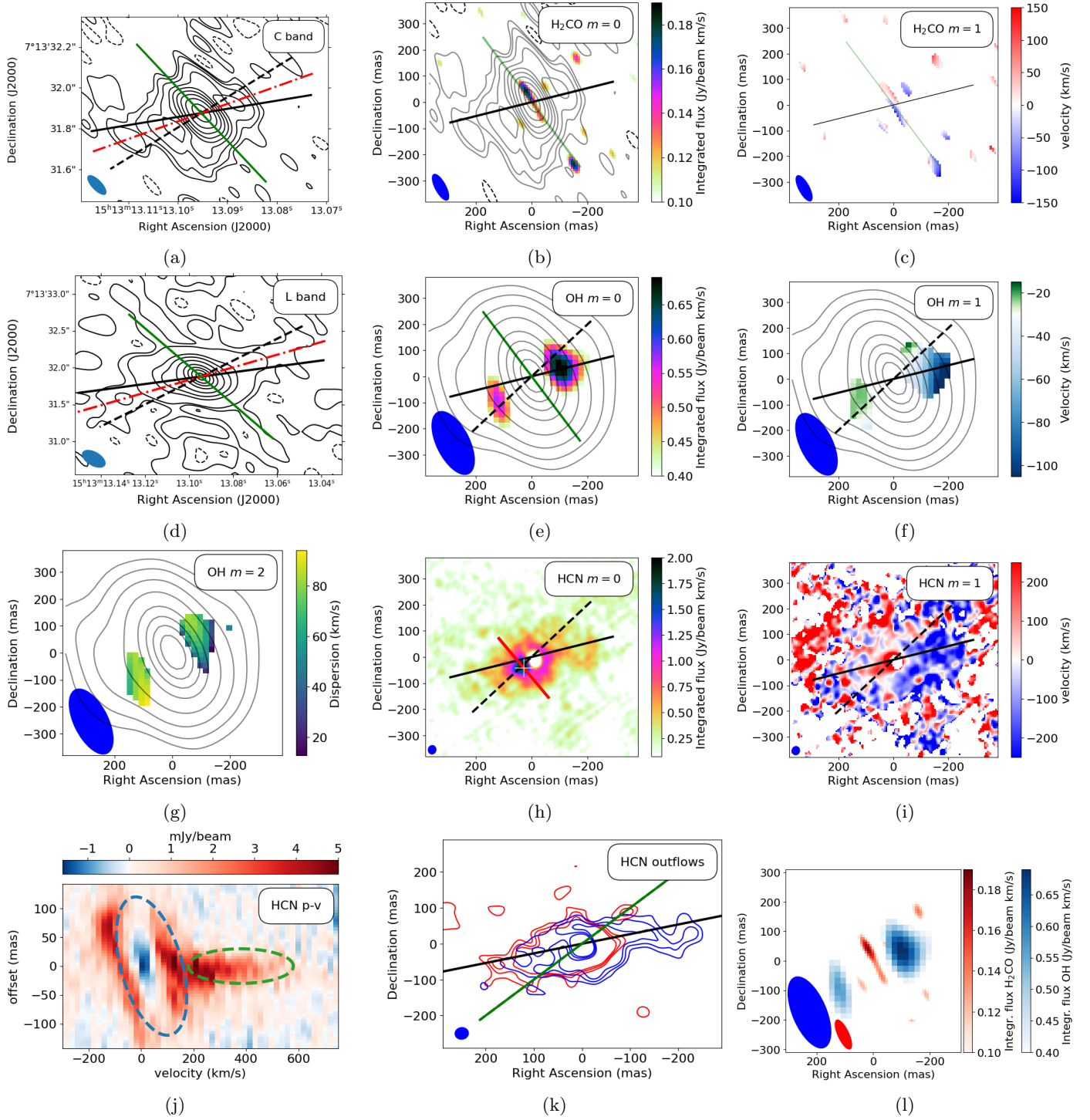[3] Typical galactic H_2CO masers have luminosities $\lesssim 10^{-6}$ $L_\odot$.

Fig. 1: e-MERLIN and ALMA observations toward the nuclear region of Zw049.057. (a) e-MERLIN C band continuum contour map. Contour levels: $[-1, 1, 3, 30, 60, 120, 240, 360, \ldots]\sigma$, with $\sigma = 3.56 \times 10^{-5}$ Jy/beam. The dashed contour corresonds to -1σ. (b,c) H_2CO 4.83 GHz emission moment 0 (b) and 1 (c) map overlaid (b) with C Band continuum emission contour map. (d) e-MERLIN L Band continuum emission contour map. Contour levels: $[-1, 1, 3, 6, 12, 24, 48, 96, 384, \ldots]\sigma$, with $\sigma = 7.70 \times 10^{-6}$ Jy/beam. (e,f,g) OH megamaser emission (1.667 GHz) moment maps (e, moment 0; f, moment 1; g, square root of the moment 2). Images are overlaid with L band continuum emission contours. (h,i) Moment 0 (h) and moment 1 (i) maps of the HCN $J = 3 \rightarrow 2$ emission. In (h), negative emission yields (absorption) are put to zero. Red line and white mark in (h) indicate the slice and center of the p-v diagram shown in (j). (k) Integrated intensity of HCN high-velocity wings. Integration performed between velocities $\pm 250 - \pm 750$ km s^{-1} (blue/red). Contour levels: $[3, 4, 5, \ldots] \times 33$ mJy/beam km s^{-1}. (l) juxtaposition of the moment 0 maps of H_2CO (red) and OH (blue) emission. Directions of the radio-jet (PA$_{jet}$ = 130°), CO outflow (PA$_{CO}$ = 105°), and disk major axis (PA$_{maj}$ = 30°) are indicated by the dashed black line, solid black line, and solid green line, respectively. Direction of the extended feature in the L-band continuum (PA$_L$ = 120°) is indicated by the dash-dotted red line. Spatial offsets of line emission maps are with respect to position of L band continuum maximum. Fitted beams are shown in the lower-left corner of the image.

Table 1: Summary of the eMERLIN observations.

	$I_{\nu,\mathrm{max}}$ (mJy beam^{-1}) [a]	S_ν (mJy) [b]	$\int \mathrm{d}v S_\nu$ (Jy km s^{-1}) [c]
L band cont.	21.5 ± 0.4	41.4 ± 4	
OH	6.50 ± 0.77		2.0 ± 0.4
C band cont.	12.0 ± 0.1	25.6 ± 2	
H_2CO	1.1 ± 0.2		0.48 ± 0.04

Notes. [a]Maximal flux density, [b]Spatially integrated flux density, [c]Spatially and spectrally integrated flux density.

3.5. HCN minor axis emission

The HCN $J = 3 \rightarrow 2$ transition was detected toward the nucleus of Zw049.057. An image of the integrated intensity is given in Fig. 1h. In the inner 50 mas (14 pc) toward the nucleus, HCN is observed in absorption, while it is observed in emission farther out from the nucleus. Emission extends farther along the minor axis (PA of ~120°, Falstad et al. 2018), compared to the major axis (PA of ~30°, Falstad et al. 2018).

We analyzed the velocity structure of the minor axis emission using a position-velocity diagram (p-v diagram) of a strong feature along the minor axis. The position-slice is perpendicular to the minor axis, and indicated in Fig. 1h, in which the zero-offset position is marked with a blue cross. The p-v diagram is plotted in Fig. 1j. In the diagram, we observe a feature that presents a correlated position-velocity structure between -150 to $200\,\mathrm{km\,s^{-1}}$, and a feature that is associated with high-velocity emission $>200\,\mathrm{km\,s^{-1}}$, extending to ~$600\,\mathrm{km\,s^{-1}}$ where we observe emission concentrated around the central position. We indicated the high-velocity feature with a green marking. Interestingly, the emission of the feature between -150 to $200\,\mathrm{km\,s^{-1}}$ follows the profile of a skewed and shifted ellipse in PV-space. The ellipse, which was fitted by eye, is drawn in dashed blue in Fig. 1j, and is $120\,\mathrm{km\,s^{-1}}$ wide and 120 mas high, shifted by $40\,\mathrm{km\,s^{-1}}$, and skewed by a velocity gradient of $0.5\ \mathrm{km\,s^{-1}\,mas^{-1}}$.

Finally, we present in Fig. 1k an integrated intensity image of the high-velocity ($\pm 250\,\mathrm{km\,s^{-1}} - \pm 750\,\mathrm{km\,s^{-1}}$) emission. Both the blueshifted and the redshifted emission show an emission structure that is concentrated along the minor axis, consistent with the earlier discussed p-v diagram. We retrieved an integrated total flux of $12.7\,\mathrm{Jy\,km\,s^{-1}}$ for the redshifted high-velocity emission and $12.5\,\mathrm{Jy\,km\,s^{-1}}$ blueshifted high-velocity emission, but note that the integrated total flux of the blueshifted emission may be an overestimation due to contamination of the $4_{1,3} \rightarrow 3_{1,2}$ methanimine line (rest frequency 266.270024 GHz) at $432\,\mathrm{km\,s^{-1}}$ with respect to the HCN $3 \rightarrow 2$ rest frequency.

4. Discussion

4.1. HCN outflow

The HCN emission along the minor axis traces two distinct structures, as can be readily ascertained from Fig. 1j. We first discuss the low velocity feature, indicated in blue in Fig. 1j. From the p-v diagram, emission could be extracted that appeared as a shifted, skewed ellipse (width: $120\,\mathrm{km\,s^{-1}}$, height: 120 mas, shift: $40\,\mathrm{km\,s^{-1}}$, skew: $0.5\,\mathrm{km\,s^{-1}\,mas^{-1}}$) in p-v space. We propose that this feature traces a rotating, wide-angle, and hollow, outflowing structure. The skew corresponds to a velocity gradient ($5.7 \times 10^{-14}\,\mathrm{s^{-1}} = 1.8\,\mathrm{km\,s^{-1}\,pc^{-1}}$) that is due to the outflow rotation. The width and shift of the ellipse are due to

emission from the front- and back side of the outflow, with a velocity directed radially from (width, $\frac{1}{2} \times 120\,\mathrm{km\,s^{-1}} = 60\,\mathrm{km\,s^{-1}}$) and along (shift, $40\,\mathrm{km\,s^{-1}}$), the outflow symmetry axis (see Appendix B of Tabone et al. 2020, for modeling of a transverse pv cut for an expanding wind annulus). We considered the possibility that the blue side of the elliptical structure represents the rotating nuclear disk, but ruled out this scenario, as the elliptical structure is present also in minor axis p-v slices $>200\,\mathrm{mas}$, beyond the HCN disk radius of ~150 mas.

Both Figs. 1j and 1k clearly indicate that the high-velocity emission emerges from a linear and confined structure. From its spatial and velocity structure, we interpret the high-velocity HCN emission along the minor axis as a fast collimated outflow. For the position angle of the collimated outflow we find $\mathrm{PA}_{\mathrm{HCN}} = 105°$. Interestingly, this is the same as the position angle that Falstad et al. (2018) find for the outflow traced by CO $J = 6 \rightarrow 5$ emission. Falstad et al. (2018) find that the CO $J = 6 \rightarrow 5$ emission extends to $400\,\mathrm{km\,s^{-1}}$, less than the ~$600\,\mathrm{km\,s^{-1}}$ we find, but this discrepancy may be due to different excitation conditions or sensitivity effects. We propose the CO $J = 6 \rightarrow 5$ emission, observed by Falstad et al. (2018) and the high-velocity HCN emission are tracing the same structure.

To estimate the mass of the fast collimated outflow, we extracted its luminosity and used the L(HCN) to M(dense) conversion relation of Gao & Solomon (2004). We note that the conversion relation of Gao & Solomon (2004) was derived for the HCN 1−0 line; to convert our HCN $3 \rightarrow 2$ luminosity to an HCN 1−0 luminosity, we assumed a HCN $\frac{J=3\rightarrow2}{J=1\rightarrow0}$ temperature ratio of 0.3 (Krips et al. 2008). Accounting only for the red outflow ($12.7\,\mathrm{Jy\,km\,s^{-1}}$, $250−500\,\mathrm{km\,s^{-1}}$), this procedure yields a collimated outflow mass of $M_{\mathrm{HCN}} = 6.2 \times 10^7\,M_\odot$. We note that the conversion relation is derived for gravitationally bound gas, so the mass will be overestimated if the dense gas is in non self-gravitating clumps. Aalto et al. (2015b) studied the impact of turbulence on the conversion factor and found that it should be scaled down by about a factor of five for non self-gravitating gas in the outflow. Because of these uncertainties, we adopt $M_{\mathrm{HCN}} = 1−6 \times 10^7\,M_\odot$ in order to compute the outflow kinematics from our mass estimates. Furthermore, we put conservative estimates of ~$250\,\mathrm{km\,s^{-1}}$ and 30 pc for the outflow velocity and size. Combined, we compute the mass-loss, momentum, momentum flux, energy and energy flux of the outflow as: $\dot{M}_{\mathrm{HCN}} = 85.2−511\,M_\odot/\mathrm{yr}$, $p_{\mathrm{HCN}} = 2.5−15 \times 10^9\,M_\odot\,\mathrm{km/s}$, $\dot{p}_{\mathrm{HCN}} = 1.3−6.5 \times 10^{12}\,L_\odot/c$, $E_{\mathrm{HCN}} = 0.8−3.9 \times 10^{55}$ ergs and $\dot{E}_{\mathrm{HCN}} = 0.5 − 2.7 \times 10^9\,L_\odot$. We note that we have not included any energy contribution from gas dispersion in our estimates for the outflow energy. In terms of the IR luminosity of Zw049.057, we may put the moment flux and energy flux, $\dot{p}_{\mathrm{HCN}}/(L_{\mathrm{IR}}/c) \approx 7−34$ and $\dot{E}_{\mathrm{HCN}}/L_{\mathrm{IR}} \approx 0.003−0.015$. These are strikingly high yields for the momentum and energy fluxes. Compared to the sample of ULIRG outflows that González-Alfonso et al. (2017)

analyzed, where outflow momentum and energy fluxes in the range of $2-5\,L_{IR}/c$ and $0.1-0.3\%\,L_{IR}$ were derived, both the energy and momentum fluxes of the outflow traced by HCN are at the higher end, or exceeding, the yields of the ULIRG outflows. We discuss this point in more detail in Section 4.3.

4.2. OHM outflow

The OHM spatial and velocity structures, showing emission along the minor axis with a velocity gradient of $\sim 100\,\mathrm{km\,s^{-1}}$, red in the SE toward blue in the NW, are consistent with an outflowing structure. We rule out that the OHM is excited in the disk, as in this scenario maximal emission is expected toward the disk major axis (Pihlström et al. 2001; Parra et al. 2005), opposite to what we observe. Indeed, with velocity dispersion of the order of the disk rotation (Falstad et al. 2018), the longest, velocity-coherent, columns of OH are expected toward the disk major axis, while Fig. 1a also shows significant seeding radiation to emerge therefrom. Yet no maser emission is observed from the disk, leading us to suggest that population inversion is suppressed there. While we cannot rule out that rotation contributes to the velocity profile of the OHM features, the observed velocity gradient cannot be explained by rotation alone. Finally, the evidence for outflowing structures emerging from the nuclear region in the HCN emission, including a structure that has similar kinematical properties as the features traced by the OHM, is additional circumstantial evidence that OHM is tracing an outflow structure. Thus, we interpret the OHM emission as emerging from an outflow structure.

We proceed to make kinematical estimates of the OHM outflow. In order to estimate the OHM outflow mass, we use the result that OHM operate around OH column densities of $N_{OH} \sim 10^{17}\,\mathrm{cm^{-2}}$ (Lockett & Elitzur 2008). We define the OHM emission region as the one where the spectrally integrated intensity exceeds $0.3\,\mathrm{Jy/beam\,km\,s^{-1}}$, which has an angular area of $0.12\,\mathrm{arcsec^2}$. Using an abundance of $x_{OH} = 2 \times 10^{-6}$ (González-Alfonso et al. 2012, 2017) relative to H_2, and an average particle mass of $\mu = 2.3\,m_H$, we compute the OHM outflow mass as $M_{OHM} = 9 \times 10^6\,M_\odot$. Adopting an outflow velocity of $50\,\mathrm{km\,s^{-1}}$ and a size of 30 pc, the mass expulsion rate of the outflow is $\dot{M}_{OHM} = 15\,M_\odot/\mathrm{yr}$. With these estimates, we compute the momentum, momentum flux, energy and energy flux of the outflow as: $p_{OHM} = 8.8 \times 10^{46}\,\mathrm{g\,cm\,s^{-1}}$, $\dot{p}_{OHM} = 3.7 \times 10^{10}\,L_\odot/c$, $E_{OHM} = 2.187 \times 10^{53}\,\mathrm{ergs}$ and $\dot{E}_{OHM} = 3.1 \times 10^6\,L_\odot$. In terms of the IR luminosity of Zw049.057, we may put the moment flux and energy flux, $\dot{p}_{OHM}/(L_{IR}/c) = 0.2$ and $\dot{E}_{OHM}/L_{IR} = 2 \times 10^{-6}$.

The OHM outflow velocity ($50\,\mathrm{km\,s^{-1}}$) is much less than the minimal velocity required to escape the inner region ($\sqrt{2}v_{circ} \approx 200\,\mathrm{km\,s^{-1}}$, see, e.g. Martin 2005). Indeed, as discussed in Section 4.3, the OHM outflow will likely fail to escape the inner region and will be obscured when observed in the IR range of the spectrum. Instead, the outflow will likely fall back onto the gas close to the nuclear region, causing a significant stirring of the nuclear gas (Aalto et al. 2020; Wada 2012). Not only will the nuclear gas be endowed an appreciable amount of kinetic energy in the form of turbulence, but the gas stirring will also impact the accretion dynamics significantly, as turbulence is directly related to the effective viscosity of the gas (Shakura & Sunyaev 1976; Pringle 1981). CON regions are consistently associated with nuclear gas velocity widths in excess of $100\,\mathrm{km\,s^{-1}}$. If this is dispersion, it would imply that the turbulent kinetic energy of the gas far exceeds the thermal energy: $E_{kin}/E_{therm} > 10^4$. It may therefore well be possible, at least locally, that the conversion of

turbulent energy through shocks may be a significant source of luminosity. We however note that the flows may still be largely laminar and that the high velocity widths are caused by line of sight effects of a layered structure of in- and outflows.

Spectroscopic IR observations, performed with Herschel, at 23 H_2O and 12 OH transitions, have not been able to definitively indicate the outflow we observe in the OHM emission (Falstad et al. 2015). This is partially due to resolution and the relatively low outflow velocity of the OH gas. But, also, and importantly, we find clear evidence that the OHM emission is excited only in the outflowing gas. Thus revealing a map of the outflowing gas that is relatively uncontaminated by the disk emission. While we present the first resolved interferometric maps of OHM in association with an outflow, spectral features that were offset in velocity gave early indications in single dish observations of Zw049.057 (Baan et al. 1987) and other OHM galaxies (Baan et al. 1989). Notably, through spectral analysis, Gowardhan et al. (2018) were able to find striking evidence of the association of OHM with outflowing gas toward two ULIRGs, by combining unresolved OHM observations with interferometric imaging of CO and CN emission. In Section 4.5.1 we discuss OHM tracing outflow structures in relation to their excitation conditions and often-observed association with H_2CO megamasers.

4.3. Outflow launching

The kinematic estimates we presented above may help us to constrain the launching mechanism of the high-velocity collimated outflow and the slow wide-angle outflow. First, we consider the scenario of a radiatively driven outflow. Radiation pressure is a momentum conserving mechanism to launch the outflows. We compare the total momentum flux of the outflow components and relate it to the momentum flux that emanates from the nuclear region. For the OHM outflow, we estimated earlier $\dot{p}_{OHM}/(L_{IR}/c) = 0.04-0.2$, while for the collimated HCN outflow, we estimated $\dot{p}_{HCN}/(L_{IR}/c) \approx 7-34$. Thus, without a significant momentum boost, it is difficult to explain the collimated HCN outflow with a momentum conserving outflow launching mechanism.

It is possible for the wide-angle outflow to be radiatively driven. We explore the hypothesis that the slow wide-angle outflow traced by OHM is radiatively launched. First, the OHM clumps have significant column densities, which ensure continuum optical depths of order unity, even for long wavelengths. Indeed, with optical depths $\tau_{OHM} \sim 1$ at 10 μm (corresponding to the maximal specific intensity of thermal radiation of $\sim 300\,\mathrm{K}$), it is a possibility that the OHM clumps are lifted from the CON surface by the thermalized IR radiation field. At the instance of our observations, the OHM outflow has attained a (projected) velocity of $v_{OHM} \approx 50\,\mathrm{km\,s^{-1}}$. It is interesting to speculate about the progression of the outflow launching, assuming it is radiatively driven. If the outflow is to be accelerated, we require the outward force on an OHM clump, which is due to the radiation field, to exceed the inward force due to gravity. We follow Heckman et al. (2015) and define the outward force due to the radiation field as $F_{out} = \dot{p}_{rad}A_c/4\pi r^2$, where $\dot{p}_{rad}$ is the radiation momentum flux, A_c is the cloud area and r is the distance from the nucleus. The inward force due to gravity we put at $F_{in} = M_{OHM}v_{cir}^2/r$, where M_{OHM} is the OHM clump mass and v_{cir} is its circular velocity. The critical momentum flux to drive an OHM clump outwards can be obtained by equating the inward and outward forces and is $\dot{p}_{crit} = 2.1 \times$

$10^{11} L_\odot / c \left(\frac{r}{30\,\mathrm{pc}} \right) \left(\frac{N_{\mathrm{OHM}}}{3 \times 10^{22}\,\mathrm{cm}^{-2}} \right) \left(\frac{v_{\mathrm{circ}}}{140\,\mathrm{km\,s}^{-1}} \right)^2$, adopting typical values for the OHM clumps that occur in the outflow as we observe it. Interestingly, the critical momentum flux is similar to L_{IR}/c. This indicates that if the radiation is the driving agent, the OHM outflow is not accelerating. In fact, after numerical integration of the above equations, adopting the cited typical values for the OHM clumps that occur in the outflow as we observe it, we found that after $\sim 4 \times 10^5$ years, the outflowing OHM clumps will acquire a negative velocity, indicating that they will evolve to fall back onto the galactic disk as a fountain flow (Wada 2012).

The collimated HCN outflow requires a driving mechanism beyond radiation, due to the high momentum requirements. First, the possibility has been explored that the molecular outflow of Zw049.057 as traced by CO $J = 6 \rightarrow 5$ emission, which is likely the same outflow as traced by the high-velocity HCN emission, is entrained by a radio jet (Falstad et al. 2018). Indeed, Falstad et al. (2018) find that the radio continuum around 5.3 GHz shows an extended feature along the minor axis, and while this possible radio jet is not aligned with either the HCN or the CO outflow found by Falstad et al. (2018), it may still have powered them and deflected. Based on the jet power estimate, $\dot{E}_{\mathrm{jet}} = 4.7 \times 10^9\,L_\odot \approx \dot{E}_{\mathrm{HCN}}$ (Falstad et al. 2018; Baan & Klöckner 2006; Bîrzan et al. 2008), we do not rule out the (tentatively detected) radio-jet as a driver of the dense collimated outflow, but we do note that our estimates for the energy flux are likely lower limits, as we have not included the velocity dispersion in the outflow energy estimate, and we use a projected velocity for the outflow velocity. Alternatively, the molecular outflow that we observe can be entrained by an energy driven AGN wind (Silk & Rees 1998; Aalto et al. 2012, 2015a). If this is the case, we expect the collimated outflow to be associated with an ionized and hot wind. In addition, in order for the molecular material not to be disrupted by the entrainment, rapid radiative cooling and/or stabilizing magnetic fields are required (Cooper et al. 2009; McCourt et al. 2015; Leaman et al. 2019).

The projected outflow velocity of the dense collimated outflow traced by HCN was put at >200 km s^{-1}, with maximal projected velocities approaching 650 km s^{-1}. These outflow velocities are comfortably larger than $\sqrt{2}v_{\mathrm{circ}} \approx 200$ km s^{-1}, suggesting that this outflow will escape the nuclear region. Outflow velocities in excess of $3v_{\mathrm{circ}} \approx 420$ km s^{-1} are required to escape the galaxy (Martin 2005), which thus appears to be the fate of a significant fraction of this outflow.

It has been suggested that the morphology and kinematics of CON regions resemble the protostellar environment (Aalto et al. 2020; Gorski et al. 2023). In protostellar regions, outflows are thought to be launched magnetocentrifugally (Blandford & Payne 1982; Pelletier & Pudritz 1992; Wardle & Koenigl 1993; Spruit 1996; Tabone et al. 2020), and magnetically collimated. The outflow takes the appearance of a fast collimated jet-like structure, emerging from the inner launching regions, while toward the outer launching regions, a wide(r)-angle and lower velocity outflow emerges (Spruit 1996; Tabone et al. 2020). Such an appearance is both consistent with the dynamics and chemistry we find for our outflows, but we note that this mechanism operates most effectively when gas flows are laminar and critically depends on the presence of an ordered magnetic field.

Magnetic fields in cool molecular gas may either be probed through dust polarization observations (Andersson et al. 2015), or through spectral line polarization, either through the Zeeman effect (Crutcher et al. 1993; Lankhaar & Teague 2023) or through the Goldreich-Kylafis effect (Goldreich & Kylafis 1981;

Lankhaar & Vlemmings 2020). Unfortunately, continuum emission is heavily affected through self-absorption and scattering effects in buried regions (González-Alfonso & Sakamoto 2019), even at (sub)millimeter wavelengths. With OHM tracing the outflow, observation of its circular polarization would lead to constraints on the magnetic field in these regions. Such extragalactic Zeeman observations of OHM have been performed previously (Robishaw et al. 2008), on a sample of OHM sources exhibiting strong emission. For the Zw049.057 OHM, with its modest intensity yields, Zeeman observations will require very deep integration, which would be beyond feasibility for the current radio telescopes, but may become possible with the next generation of radio observatories such as the SKA. Alternatively, it may be possible to attain magnetic field information toward the nuclear region through linear polarization observations of vibrationally excited HCN emission, which is known to be luminous (Falstad et al. 2021) and expected to be significantly polarized due to its radiative excitation (Lankhaar & Vlemmings 2020; Lankhaar et al. 2022).

4.4. Inner dynamics of Zw049.057

Based on the spatial and velocity signatures of the H$_2$CO megamaser, OH megamaser and HCN emission, as well as constraints from excitation modeling that we discuss in Section 4.5.1, we propose the following model of the dense gas surrounding the nucleus of Zw049.057. Fig. 2 presents a cartoon of the dense gas surrounding the nucleus of Zw049.057. In this model the H$_2$CO megamaser is tracing the nuclear disk[4]. The OH megamaser is not excited toward the nuclear disk, but rather, we propose, in a wide-angle and slow moving outflow structure. The OHM outflow envelopes a denser, faster, and collimated outflow that is traced by high-velocity HCN emission. This is likely the same outflow that Falstad et al. (2018) detected in CO $J = 6 \rightarrow 5$ emission at lower resolution. As discussed in Section 4.3, we estimate that the dense collimated outflow has likely attained sufficient velocity to escape, at least, the nuclear region. In contrast, the wide-angle outflow traced by the OH megamaser does not possess sufficient velocity to escape the nuclear region. Instead, we expect the wide-angle outflow to be drawn back to the nuclear disk after ~ 1 Myr to form a so-called fountain flow (Wada 2012).

4.5. OH megamasers

4.5.1. OH megamaser excitation

It is interesting to compare our observations of the 1.667 GHz OHM to existing observations of OH toward Zw049.057. Falstad et al. (2018) observed the OH 4.660 GHz, 4.766 GHz and 4.751 GHz hyperfine transitions in absorption toward the nucleus of Zw049.057. Of these transitions, the 4.751 GHz is the main hyperfine transition, while the transitions at 4.660 GHz and 4.766 GHz are satellite hyperfine transitions. The relative intensities of these three hyperfine transitions are (4.660:4.751:4.766) GHz = (1:2:1) in the optically thin limit,

---

[4] Our imaging of H$_2$CO maser emission toward Zw049.057 agrees very well with the imaging performed by Baan et al. (2017) using MERLIN. Yet, Baan et al. (2017) find for other H$_2$CO megamaser galaxies other configurations of H$_2$CO maser emission, which does not seem to be exclusively tracing the nuclear disk. In the absence of interferometric data to a larger sample of H$_2$CO megamaser galaxies, we do not intend to make the general claim that H$_2$CO megmaser emission traces the nuclear disk of the host galaxy.
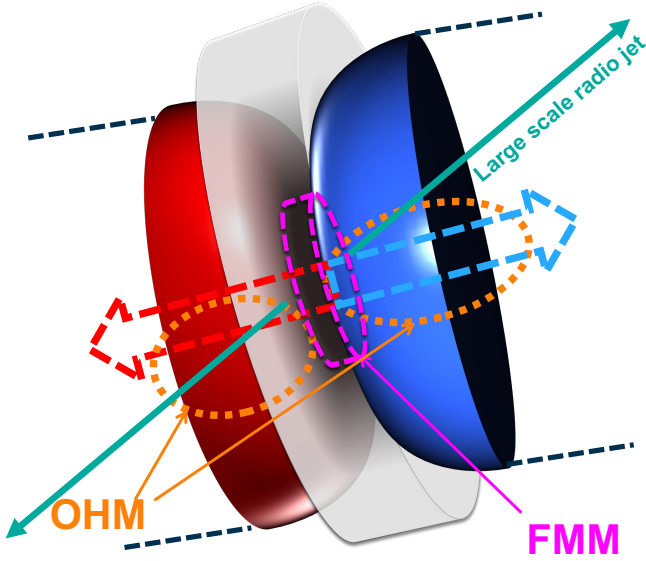
Fig. 2: Cartoon of nuclear system of Zw49.057. The collimated dense outflow that is traced by the high-velocity HCN emission is indicated with dashed red and blue arrows. Rotating wide-angle wind as traced by the lower velocity HCN emission is indicated by the hollow bi-spheres. Dotted lines are added to the ends of the hollow bi-cones to indicate their extension further out. The outflowing OH megamaser emission is excited toward the regions indicated by dotted orange ellipses. H_2CO megamaser emission (FMM) is excited in the inner regions of the nuclear disk, indicated by dotted magenta. We have furthermore drawn the extended nuclear disk in semitransparent gray-scale, as well as the large-scale radio jet, that is differently inclined from the outflow system traced by HCN and OH.

under local thermodynamic equilibrium (LTE; Destombes et al. 1977). The relative peak absorption of the lines follow the ratio expected under LTE. However, different line profiles were found among the transitions, which was interpreted as the result of OH gas that is excited under varying conditions, comprising the signal (Falstad et al. 2018). Furthermore, Falstad et al. (2018) found that the spatially and kinematically resolved emission from the 4.751 GHz transition, indicate that the dominant part of the emission emerges from a rotating structure along the major axis, while they found tentative evidence for a feature at ~200 km s^{-1} to the northwest of the continuum peak. McBride et al. (2013) observed the satellite transitions associated with the 1.67 GHz OHM at 1.612 and 1.712 GHz using the Arecibo telescope. From the conjugate line profiles of the OHM satellite lines, they concluded that two separate inversion mechanisms exist in Zw049.057.

Earlier, we showed that the OHM appears in an outflowing structure along the galactic minor axis. The OH outflow appears to envelop a collimated and dense outflow traced by high-velocity HCN emission. While OH is observed toward the nuclear disk in its 6 cm and far-IR lines (Falstad et al. 2015, 2018), we detect it there neither as a maser nor in absorption in the 1.667 and 1.665 GHz transitions. This, while H_2CO is observed as a megamaser in association with the nuclear disk. The combination of these observations confirms earlier conjectures that distinct excitation mechanisms or regions exist for the OH emission toward Zw049.057 (McBride et al. 2013; Falstad et al. 2018).

The presence and absence of OHM and H_2CO maser emission allows us to constrain the excitation conditions in the outflow and nuclear region of Zw049.057. It is well established that OH megamasers appear in association with FIR radiation around 53 μm absorbed through the OH $^2\Pi_{\frac{1}{2}}-^2\Pi_{\frac{3}{2}}$ $J = \frac{3}{2} - \frac{3}{2}$ transitions, which causes population inversion in the transitions around 1.67 GHz through radiative pumping (Lockett & Elitzur 2008). Population inversion is achieved in turbulent clumps ($\Delta v \sim 20$ km s^{-1}) of sizes $\lesssim 1$ pc, number densities $\lesssim 10^5$ cm^{-3} and specific OH column densities of the order 10^{16} cm^{-2}km^{-1}s. For such clumps, maser optical depths $\tau_{1.667\,GHz} \sim -1$ are expected (Lockett & Elitzur 2008). A bright (nonthermal) background radiation field around 18 cm wavelengths is required for OH megamasers to be apparent, while multiple maser clumps along the line-of-sight may boost the amplification of this background radiation significantly (Parra et al. 2005). Detailed modeling of the excitation of H_2CO masers finds that the 4.8 GHz H_2CO maser is excited toward denser regions $\gtrsim 10^5$ cm^{-3}, where the maser pumping is collisional (van der Walt & Mfulwane 2022). Maser pumping can operate in environments with a prominent FIR radiation field, provided the gas temperature exceeds the radiation temperature (van der Walt & Mfulwane 2022). A rather restrictive constraint that van der Walt & Mfulwane (2022) put to the operation of H_2CO masers, is that it requires H_2CO to be present in high abundance ($x_{H_2CO} \sim 10^{-5}$). Such H_2CO abundances are 3 to 4 orders of magnitude higher than what is typically found toward Galactic star forming regions, hot cores or dark clouds (see, e.g., Mangum & Wootten 1993; Tang et al. 2018; Kirsanova et al. 2021). We note, that the abundance constraint was formulated for H_2CO masers excited toward high-mass star-forming regions. For H_2CO megamasers, velocity-coherence length scales, ℓ, can be two orders of magnitude higher, while line-widths, Δv, are one order of magnitude higher. Thus, taking into consideration that (large-velocity gradient) radiative transfer problems depend primarily on the specific column density, $x_{H_2CO}n_{H_2}\ell/\Delta v$, the abundance requirements are relaxed by about an order of magnitude. Still, taking this into consideration, H_2CO abundance requirements seem too high, and we suggest dedicated modeling of H_2CO megamaser sources is required to address this issue.

We suggest that the absence of OH emission or absorption around 1.67 GHz in the nuclear disk is the consequence of the high densities in these regions, that effectively suppress the maser mechanism. Instead, because of the outflow expansion, OH clumps in the outflow structure are more tenuous, allowing thus for efficient maser pumping. In addition, for the OHM to operate, one requires efficient FIR pumping. The FIR radiation in the OH outflow may either emerge from the CON region, or from the collimated denser part of the outflow that is traced by high-velocity HCN emission, and which the OH outflow envelops. While the CON region subtends a large solid angle as seen from the OH outflow, absorption may diminish its prominence. On the other hand, considering the lifetime (~10^5 years) of the collimated outflow, we require a mechanism such as star formation in this region to heat up the dust phase, to account for the emergence of FIR radiation here from.

4.5.2. The class of OH megamasers and CONs

A synthesis of the OHM surveys by Baan (1989) and Darling & Giovanelli (2002) and the host galaxy IR, CO and HCN luminosities, indicate an association between OHM and high molecular gas densities and fractions, as well as an unusual

IR-CO luminosity relation (Darling 2007). On the basis of this, it is suggested that OHM are associated with a compact and intense mode of star formation that is likely triggered by tidal density enhancements due to merger events (Darling 2007). This picture is consistent with modeling efforts (Parra et al. 2005; Lockett & Elitzur 2008), and are not in tension with previous high resolution imaging of the OHM using VLBI instruments (Lonsdale et al. 1998; Pihlström et al. 2001; Richards et al. 2005), that were performed on, primarily, the more luminous OHM. However, our high-resolution observations of the OHM emission that show the association with an outflowing structure toward the LIRG Zw049.057, require a more subtle picture of the class of OHM.

We pointed out earlier that Zw049.057 is a CON, a subclass of (U)LIRGs that host exceptionally dense nuclear regions and are associated with both inflow and outflow motions. While only a small fraction ($\lesssim 10\%$) of LIRGs, and up to a third of ULIRG galaxies host OHM (Darling & Giovanelli 2002), almost all LIRG and ULIRG CON galaxies that have been searched for OHM emission, indeed host OHM. At first, this is not surprising, as OHM are associated with high density gas (Darling 2007), and show prominent absorption in OH around $53\,\mu m$, which is a requisite for OH maser pumping (González-Alfonso et al. 2012, 2015). Yet, of the known H_2CO megamasers, 5/6 are hosted by CONs, of which 1 of them is a ULIRGs (Arp 220) and the 4 others are LIRGs (IC 860, UGC 5101, IRAS 17578–0014, Zw049.057), where each of them is additionally associated with OH maser emission. The association of the OHM with H_2CO megamaser appears problematic, as only very limited conditions allow for the simultaneous excitation of both H_2CO and OH megamasers. Our high-resolution interferometric observations show that the issue of the apparent association between OHM and H_2CO megamaser emission can be resolved, as they emerge from different regions; outflow (OHM) and nuclear disk (H_2CO megamaser) structures. We speculate that a similar arrangement may be present for the other LIRGs that host OH and H_2CO megamaser.

4.6. OH megamasers at high redshift

Untargeted HI surveys directed to distant objects, are often sensitive to OH maser lines, too (Briggs 1998). While OHM detections in HI surveys may be seen as contaminations, using spectroscopic redshifts if available, or more elaborate methods using the host galaxy continuum properties, OHM galaxies may be positively identified and isolated from these HI surveys (Roberts et al. 2021). Indeed, ongoing HI surveys are rapidly adding to the known sample of OHM galaxies (Blyth et al. 2016; Hess et al. 2021; Glowacki et al. 2022; Jarvis et al. 2024), and will likely triple the number of known OHM galaxies (Roberts et al. 2021). Furthermore, planned HI surveys using the next-generation of radio telescopes, that will sample galaxies at even higher redshift, will likely increase the number of known OHM galaxies by some orders of magnitude (Roberts et al. 2021). With this expected surge in OHM detections in distant galaxies, it is natural to discuss the implications of the current study. From the interferometric mapping of the OHM toward Zw049.057, our main finding is its association with an outflow, and the suppression of emission toward the nuclear disk. The outflow traced by OHM is expanding at a low velocity ($\sim 100\,km/s$), making it difficult to detect spectroscopically. This is in contrast to other studies that have associated OHM with outflows (Baan et al. 1989; Gowardhan et al. 2018; Glowacki et al. 2022), that found OHM emission at large ($200-1000\,km/s$) off-

sets from the systemic velocity. The luminosity of the OHM of Zw049.057 ($10.1 \pm 2.0\,L_\odot$) is on the lower end of the range of OHM luminosities. This feature can be ascribed to (i) Zw049.057 being a LIRG, with a naturally weaker radio-continuum that is to be amplified by OHM, (ii) the slight offset of the OHM from the continuum maximum, and (iii) the relatively small region that is conducive to population inversion. In particular, points (ii) and (iii) are a direct consequence of OHM tracing an evolved outflowing structure.

A useful feature of the untargeted HI surveys, is their broadband scanning. Thus, it is likely that for an OHM galaxy, not only the main OHM lines at $1.67\,GHz$ will be detected, but also satellite transitions at 1612 and 1720 MHz. A comprehensive analysis of the different transitions can reveal properties of the (pumping) conditions toward the OHM galaxy (Baan et al. 1987). Such an analysis has already been productively applied by Hess et al. (2021) to an OHM found in the HI survey AWES (Apertif Wide-area Extragalactic imaging Survey). For Zw049.057, analysis of the OHM lines and their satellites, revealed the presence of different pumping conditions for the OHM; a feature which we can confirm through our interferometric observations. Multiline analysis of the OHM lines and their satellites will reveal important information on the pumping conditions, but to formulate rigorous relations that reveal the OHM association with an outflow, more interferometric studies such as this one are necessary. To direct additional interferometric studies, we have pointed to H_2CO megamaser emission as a marker for OHM galaxies with OHM emission tracing outflow structures, similar to Zw049.057.

5. Conclusions

We present high-angular resolution interferometric observations of the kinematics of the nuclear region of Zw049.057. Using e-MERLIN, we observed the H_2CO and OH megamasers, and using ALMA, we observed HCN $3 \rightarrow 2$ emission. The H_2CO megamaser traces the nuclear disk, while the OH megamaser traces a slow and wide-angle outflow. The slow and wide-angle OHM outflow in turn appears to envelop a fast and collimated outflow that is traced by high-velocity HCN emission.

Momentum estimates indicate that the OH megamaser outflow may be radiatively launched, while the fast and collimated molecular outflow traced by HCN requires an additional momentum boost. Such a momentum boost may be achieved if the outflow is entrained by an energy-conserving AGN wind, or through a magneto-hydrodynamical launching mechanism. From the low velocity of the OHM outflow and an analysis of the driving forces, we conclude that the wide-angle OHM will likely not reach escape velocity, and instead evolve as a fountain flow.

We observed the H_2CO and OH megamaser to be associated with different physical structures. The excitation of OH and H_2CO megamasers require different conditions, that are almost mutually exclusive, yet of the known H_2CO megamasers, all of them have been found toward OH megamaser galaxies. Additionally, five of the six known H_2CO megamasers are found toward CONs. Since the prime characteristic of CONs is dense nuclear gas, and they are commonly associated outflow systems, we speculate that a similar arrangement can be expected for the OH-H_2CO (hydroxyl-formaldehyde) megamaser galaxies.

Our high-angular resolution interferometric observations have revealed multiple phases of outflowing gas emanating from the inner ($\lesssim 10\,pc$), and obscured ($N_{H_2} \sim 10^{25}\,cm^{-2}$), nuclear regions of Zw049.057. While the ultimate driving mechanisms of the outflowing gas phases remain ambiguous, it is clear that

they impact the gas dynamics and mass and angular momentum budget of the nuclear region greatly.

References

Aalto, S., Garcia-Burillo, S., Muller, S., et al. 2012, A&A, 537, A44
Aalto, S., Garcia-Burillo, S., Muller, S., et al. 2015a, A&A, 574, A85
Aalto, S., Martín, S., Costagliola, F., et al. 2015b, A&A, 584, A42
Aalto, S., Muller, S., König, S., et al. 2019, A&A, 627, A147
Aalto, S., Falstad, N., Muller, S., et al. 2020, A&A, 640, A104
Andersson, B., Lazarian, A., & Vaillancourt, J. E. 2015, ARA&A, 53, 501
Araya, E., Baan, W. A., & Hofner, P. 2004, ApJS, 154, 541
Baan, W. A. 1989, ApJ, 338, 804
Baan, W., & Klöckner, H.-R. 2006, A&A, 449, 559
Baan, W. A., Henkel, C., & Haschick, A. D. 1987, ApJ, 320, 154
Baan, W. A., Haschick, A. D., & Henkel, C. 1989, ApJ, 346, 680
Baan, W. A., An, T., Klöckner, H.-R., & Thomasson, P. 2017, MNRAS, 469, 916
Barcos-Muñoz, L., Aalto, S., Thompson, T. A., et al. 2018, ApJ, 853, L28
Bean, B., Bhatnagar, S., Castro, S., et al. 2022, PASP, 134, 114501
Bîrzan, L., McNamara, B., Nulsen, P., Carilli, C., & Wise, M. 2008, ApJ, 686, 859
Blandford, R., & Payne, D. 1982, MNRAS, 199, 883
Blyth, S. L., Baker, A. J., Holwerda, B. W., et al. 2016, Proc. Sci., MeerKAT Science: On the Pathway to the SKA, 25-27 May, 2016, Stellenbosch, South Africa, 4
Briggs, F. H. 1998, A&A, 336, 815
Cooper, J. L., Bicknell, G. V., Sutherland, R. S., & Bland-Hawthorn, J. 2009, ApJ, 703, 330
Crutcher, R., Troland, T., Goodman, A., et al. 1993, ApJ, 407, 175
Darling, J. 2007, ApJ, 669, L9
Darling, J., & Giovanelli, R. 2002, AJ, 124, 100
Destombes, J. L., Marliere, C., Baudry, A., & Brillet, J. 1977, A&A, 60, 55
Donnan, F., Rigopoulou, D., García-Bernete, I., et al. 2023, A&A, 669, A87
Falstad, N., González-Alfonso, E., Aalto, S., et al. 2015, A&A, 580, A52
Falstad, N., Aalto, S., Mangum, J., et al. 2018, A&A, 609, A75
Falstad, N., Hallqvist, F., Aalto, S., et al. 2019, A&A, 623, A29
Falstad, N., Aalto, S., König, S., et al. 2021, A&A, 649, A105
Gao, Y., & Solomon, P. M. 2004, ApJS, 152, 63
García-Bernete, I., Rigopoulou, D., Aalto, S., et al. 2022, A&A, 663, A46
Glowacki, M., Collier, J. D., Kazemi-Moridani, A., et al. 2022, ApJ, 931, L7
Goldreich, P., & Kylafis, N. D. 1981, ApJ, 243, L75
González-Alfonso, E., & Sakamoto, K. 2019, ApJ, 882, 153
González-Alfonso, E., Fischer, J., Graciá-Carpio, J., et al. 2012, A&A, 541, A4
González-Alfonso, E., Fischer, J., Sturm, E., et al. 2015, ApJ, 800, 69
González-Alfonso, E., Fischer, J., Spoon, H., et al. 2017, ApJ, 836, 11
Gorski, M., Aalto, S., König, S., et al. 2023, A&A, 670, A70
Gowardhan, A., Spoon, H., Riechers, D. A., et al. 2018, ApJ, 859, 35
Heckman, T. M., Alexandroff, R. M., Borthakur, S., Overzier, R., & Leitherer, C. 2015, ApJ, 809, 147
Hess, K. M., Roberts, H., Dénes, H., et al. 2021, A&A, 647, A193
Hughes, D. H., Serjeant, S., Dunlop, J., et al. 1998, Nature, 394, 241
Jarvis, M. J., Heywood, I., Jewell, J., et al. 2024, MNRAS, 529, 3484
Katgert, P., Mazure, A., Den Hartog, R., et al. 1998, A&AS, 129, 399
Kirsanova, M. S., Punanova, A. F., Semenov, D. A., & Vasyunin, A. I. 2021, MNRAS, 507, 3810
Konigl, A., & Kartje, J. F. 1994, ApJ, 434, 446
Krips, M., Neri, R., García-Burillo, S., et al. 2008, ApJ, 677, 262
Lankhaar, B., & Teague, R. 2023, A&A, 678, A17
Lankhaar, B., & Vlemmings, W. 2020, A&A, 636, A14
Lankhaar, B., Vlemmings, W., & Bjerkeli, P. 2022, A&A, 657, A106
Leaman, R., Fragkoudi, F., Querejeta, M., et al. 2019, MNRAS, 488, 3904
Lockett, P., & Elitzur, M. 2008, ApJ, 677, 985
Lonsdale, C. J., Lonsdale, C. J., Diamond, P. J., & Smith, H. E. 1998, ApJ, 493, L13
Mangum, J. G., & Wootten, A. 1993, ApJS, 89, 123
Martin, C. L. 2005, ApJ, 621, 227
McBride, J., Heiles, C., & Elitzur, M. 2013, ApJ, 774, 35
McCourt, M., O'Leary, R. M., Madigan, A.-M., & Quataert, E. 2015, MNRAS, 449, 2
Moldon, J. 2021, Astrophysics Source Code Library [record ascl:2109]
Parra, R., Conway, J., Elitzur, M., & Pihlström, Y. 2005, A&A, 443, 383
Pelletier, G., & Pudritz, R. E. 1992, ApJ, 394, 117
Pihlström, Y., Conway, J., Booth, R., Diamond, P., & Polatidis, A. 2001, A&A, 377, 413
Pringle, J. 1981, ARA&A, 19, 137
Richards, A., Knapen, J., Yates, J., et al. 2005, MNRAS, 364, 353
Robishaw, T., & Heiles, C. 2021, The WSPC Handbook of Astronomical Instrumentation: Volume 1: Radio Astronomical Instrumentation (World Scientific), 127
Robishaw, T., Quataert, E., & Heiles, C. 2008, ApJ, 680, 981
Roberts, H., Darling, J., & Baker, A. J. 2021, ApJ, 911, 38
Sakamoto, K., Aalto, S., Costagliola, F., et al. 2013, ApJ, 764, 42
Sanders, D., & Mirabel, I. 1996, ARA&A, 34, 749
Sanders, D., Mazzarella, J., Kim, D.-C., Surace, J., & Soifer, B. 2003, AJ, 126, 1607
Shakura, N., & Sunyaev, R. 1976, MNRAS, 175, 613
Silk, J., & Rees, M. J. 1998, A&A, 331, L1
Smail, I., Ivison, R., & Blain, A. 1997, ApJ, 490, L5
Song, Y., Linden, S. T., Evans, A. S., et al. 2022, ApJ, 940, 52
Spruit, H. C. 1996, ArXiv e-prints [arXiv:astro-ph/9602022]
Tabone, B., Cabrit, S., Des Forêts, G. P., et al. 2020, A&A, 640, A82
Tang, X., Henkel, C., Wyrowski, F., et al. 2018, A&A, 611, A6
van der Walt, D., & Mfulwane, L. 2022, A&A, 657, A63
van der Walt, D., Sobolev, A., & Butner, H. 2007, A&A, 464, 1015
Veilleux, S., Maiolino, R., Bolatto, A. D., & Aalto, S. 2020, A&A Rev., 28, 1
Wada, K. 2012, ApJ, 758, 66
Wardle, M., & Koenigl, A. 1993, ApJ, 410, 218
Wethers, C. F., Aalto, S., Privon, G. C., et al. 2024, A&A, 683, A27

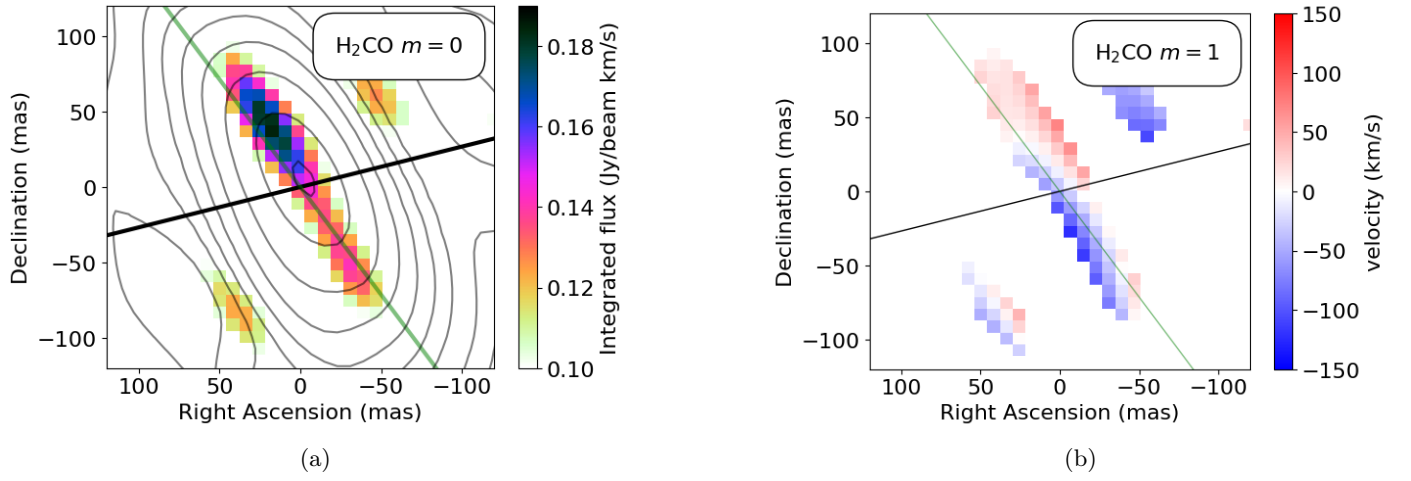# Appendix A: Additional figures

(a)

(b)

Fig. A.1: e-MERLIN observations of H_2CO 4.83 GHz emission toward the nuclear region of Zw049.057. (a) moment 0 map of the emission, overlaid with e-MERLIN C Band continuum emission contour map. (b) moment 1 map of the emission. Directions of the CO outflow ($PA_{CO} = 105°$), and disk major axis ($PA_{maj} = 30°$) are indicated by the dashed black line, solid black line, and solid green line, respectively. Figure is a zoom-in of Fig. (1b) and (1c).
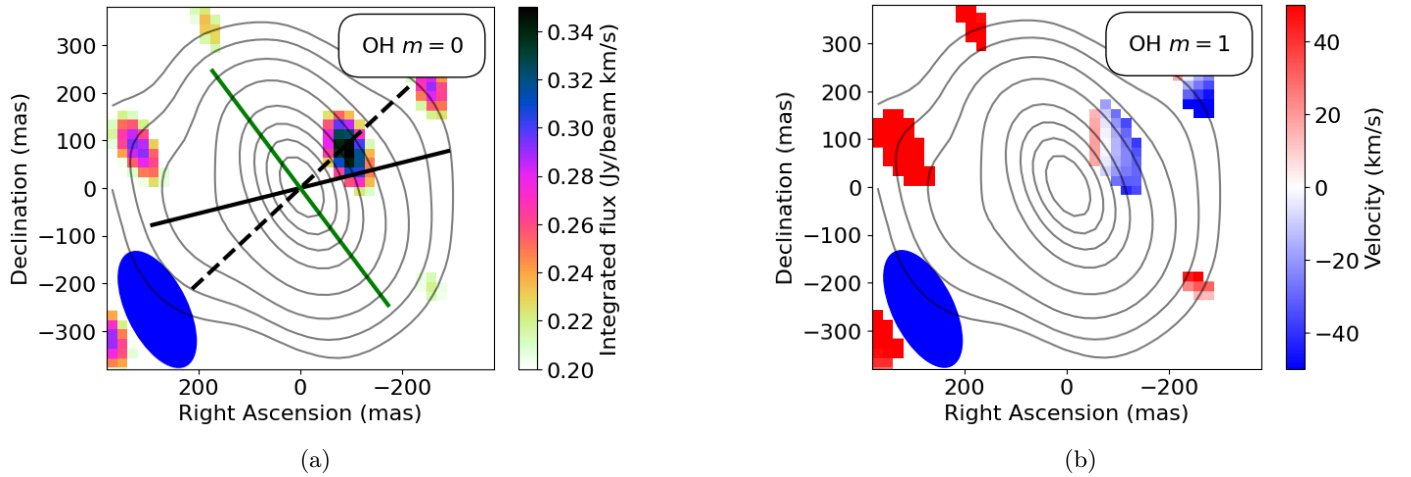

(a)

(b)

Fig. A.2: e-MERLIN observations of OH 1.665 GHz emission toward the nuclear region of Zw049.057. Moment 0 (a) and (1) maps of the emission are overlaid with e-MERLIN L Band continuum emission contour map. Directions of the radio-jet ($PA_{jet} = 130°$), CO outflow ($PA_{CO} = 105°$), and disk major axis ($PA_{maj} = 30°$) are indicated by the dashed black line, solid black line, and solid green line, respectively.